Torque Ripple Minimization of PM-assisted Synchronous Reluctance Machines via Asymmetric Rotor Poles

Torque Ripple Minimization of PM-assisted Synchronous Reluctance Machines via Asymmetric Rotor Poles

Simone Ferrari, Eric Armando and Gianmario Pellegrino
Department of Energy "*Galileo Ferraris*"
Politecnico di Torino, Turin, Italy
Email: simone.ferrari@polito.it, eric.armando@polito.it, gianmario.pellegrino@polito.it

***Abstract*—Torque ripple minimization is one of the design challenges of PM-assisted Synchronous Reluctance (PM-SyR) machines. Very often, time-consuming FEA based optimization is the preferred design strategy. Also very often, the ultimate remedy to torque ripple is to skew or step-skew the rotor of the machine, at the cost of average torque reduction. Asymmetric-pole rotors demonstrated good torque oscillation smoothing capability for Synchronous Reluctance machines; previous work showed that the Flux Barriers Shift (FBS) technique can be applied off-line to a regular design, same as skewing, with no average torque reduction. This paper extends the validity of the FBS technique to PM-SyR machines. The PM-SyR machine design flowchart is reviewed and augmented with FBS. Torque waveforms obtained with FBS and skewing are compared using FEA. Finally, the FBS design is validated against a regular design with dedicated experimental tests.**

***Index Terms*—Permanent Magnet Machines, Torque Ripple, Synchronous Reluctance Machines**

I. Introduction

Among the Permanent Magnet Synchronous Machines (PMSM), PM-assisted Synchronous Reluctance (PM-SyR) machines represent a good compromise between performance, manufacturing cost and safety. Compared to other PMSMs, PM-SyR motors show lower magnet quantity, resulting in cost reduction and increased safety in case of converter fault. Considering their performance, PM-SyR machines exhibit higher efficiency than Induction Motors (IM) and a ease of obtaining extended Constant Power Speed Range (CPSR) respect to Surface Permanent Magnet (SPM) motors. Besides all these advantages, the design of the PM-SyR machine is not yet an established process. As for many other motor types, these machines suffer of high torque ripple if not well designed, and most of optimal design techniques rely on numerical optimization, as for other Interior PM (IPM) machine types [1] - [3]. Analytical models are used in [4], [5], but they usually do not cover torque ripple minimization.

Torque ripple mitigation rules were formalized for Synchronous Reluctance (SyR) motors [6], consisting of golden rules choosing the rotor barriers pitches at the airgap, given the stator slot pitch. However, such rules are not sufficient when PMs are inserted into the rotor barriers, as the presence of the magnets also contributes to torque oscillation. The most common off-line method to reduce torque ripple is rotor skewing. Unfortunately, the substantial torque ripple reduction after skewing is associated to lower output torque, besides the more complicate manufacturing process. An alternative to skewing is to use asymmetric pole rotors. There are several ways to design asymmetric structures. Also in this case, time consuming optimization algorithms represent the common solution [7], [8]. Furthermore, some analytical approaches to the asymmetric design were studied in the past [9] - [11].

In the following, a fast design procedure for low-torque-ripple PM-SyR machine will be presented, based on Flux Barrier Shift (FBS). The design flowchart consists of three steps:

- First, a SyR machine is designed, for a torque nearly as high as the final PM-SyR machine torque target and possibly a high power factor.
- The PMs are designed according to the specified CPSR.
- Finally, torque ripple is minimized via Flux Barrier Shift.

The adopted FBS technique was recently proposed for SyR machines [12]. This method reduces the torque ripple without penalizing the average output torque and with no additional manufacturing process respect to a non skewed machine. The FBS modifies the poles in pairs, according to an angular displacement quantity. The rotor mechanical symmetry is retained, with one pole-pair periodicity instead of one pole, thus minimizing unbalanced magnetic pull [10]. The FBS benefits will be comparatively tested against skewing, using FEA. Experimental tests will compare two machine prototypes, one with regular rotor and one with FBS rotor, with asymmetric-poles. The proposed design method and FBS are included in the open-source design platform SyR-e [13].

II. Regular PM-SyR Machine Design

A. Baseline SyR Machine Design

The first step of the proposed design flowchart is the design of the baseline SyR machine. The design inputs are reported in Table I, whereas the design specifications are in Table II, referring to the final PM-SyR motor design.

The baseline SyR machine is designed according to the procedure presented in [14] referring to the maximum torque specification (43 Nm) of the PM-SyR machine. The SyR motor is normally designed for 75 - 80% of the final torque, at maximum current.

TABLE I: Design Inputs

Parameter Name	Symbol	Value
Number of pole pairs	p	2
Number of slots per pole per phase	q	3
Stator outer radius $[mm]$	R	85
Stack length $[mm]$	L	120
Airgap length $[mm]$	g	0.4
Thermal loading factor $[kW/m^2]$	k_j	3.7
Number of turns in series per phase	N_s	72
Characteristic current $[pu]$	$\frac{i_{ch}}{i_0}$	2

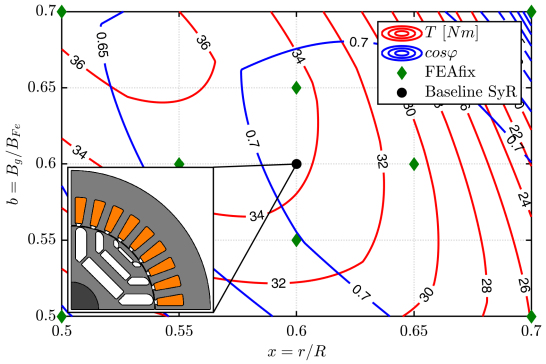

Fig. 1: Design plane used to design the baseline SyR machine.

The number and the position of the flux barriers are set to minimize the torque ripple. In the case study, the number of stator slots per pole pair is $n_s = 6q = 18$. Then, the number of equivalent rotor slots per pole pair, assuming regular pitch at the airgap, is computed as $n_r = n_s \pm 4$. The two possible configurations are $n_r = 22$ and $n_r = 14$, corresponding to 5 and 3 flux barriers, respectively. Considering that PMs will be added to the geometry, the three flux barriers solution is preferred for its simplicity.

The (x, b) design plane, proposed in [14], reports the torque T (red contours) and power factor $cos\varphi$ (blue contours) of all possible SyR motor designs having in common specifications of Table I, as a function of the rotor/stator split ratio x and the per-unit iron quantity b. The results are reported in Fig. 1. The plane is evaluated with the FEA-augmented procedure called FEAfix [14]: the eight green markers indicate the FEA-evaluated machines used for correcting the entire torque and PF maps.

It is important to select a baseline SyR machine with high torque (this reflects into the torque of the PM-SyR machine) and at the same time a high power factor, in order to reduce the amount of PM that will be needed to adjust the power factor of the PM-SyR motor design. The black circle in Fig. 1 tags the selected machine. Although this was selected for its compatibility with the stator stack available from a previous project, this design presents a good trade-off between torque and power factor as required. The cross-section of the selected baseline machine is reported at the bottom-left corner of Fig. 1.

Looking at the rotor cross section, the flux barriers thickness increase progressively from the inner to the outer layer, because these were designed for having the same permeance

TABLE II: Machine Ratings

Name	Symbol	Value
Rated current $[A_{pk}]$	i_0	22
Characteristic current $[A_{pk}]$	i_{ch}	44
Maximum current $[A_{pk}]$	i_{max}	44
DC link voltage $[V]$	V_{dc}	310
Rated speed $[rpm]$	n_0	2500
Maximum speed $[rpm]$	n_{max}	9000
Rated torque $[Nm]$	T_0	19
Maximum torque $[Nm]$	T_{max}	43
Power at maximum speed $[kW]$	$P_{n_{max}}$	11

(the more ample is also thicker). Regarding the flux carriers (rotor iron paths), their size is designed so that the total iron thickness along the rotor q axis is equal to the stator yoke length. In this way, the stator and the rotor saturate as a whole as a function of the $d-$axis current component. Alternatively, the flux barriers could be designed for being all even, which normally simplifies the bill of materials when PMs are involved.

According to the (x, b) plane plus FEAfix correction, the baseline SyR machine gives $34\,Nm$ at $44\,A$, with a $cos\varphi$ of 0.712.

B. PM Flux Linkage Design

The second step in the PM-SyR machine design is the magnets sizing, according to the principles described in [15]. The magnetic model of the PM-SyR machine (1) derives from the SyR machine theory and has the same conventions. In details, the PM flux linkage λ_m is aligned along the negative q axis, as reported in (1).

$$\begin{cases} \lambda_d = L_d \cdot i_d \\ \lambda_q = L_q \cdot i_q - \lambda_m \end{cases} \tag{1}$$

The PMs are designed so that the characteristic current of the motor i_{ch} equals the maximum current specification.

$$\lambda_m = L_q\, i_{ch} = L_q\, i_{max} \tag{2}$$

In this way, the CPRS at maximum current is infinite and the power versus speed curve is ideally flat [5]. The target ratings of the PM-SyR machine are reported in Table II.

The term $L_q\, i_{ch}$ comes from the q axis flux linkage of baseline SyR motor, when the characteristic current supplies the q axis, namely $\lambda^{SyR}_{q,i_{ch}}$:

$$\lambda^{SyR}_{q,i_{ch}} = \lambda_{ribs} + L_q\, i_{ch} \tag{3}$$

The term λ_{ribs} represents the flux linkage leakage drained by the structural ribs. Substituting (3) in (2), the PM flux linkage value is computed as:

$$\lambda_m = \lambda^{SyR}_{q,i_{ch}} - \lambda_{ribs} \tag{4}$$

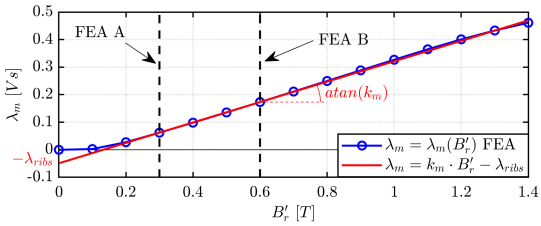

Fig. 2: PM flux linkage versus PM remanence: FEA-evaluated curve in blue and linearized characteristic (5) in red. The two simulation points to compute the linearized curve are reported in dashed black lines.

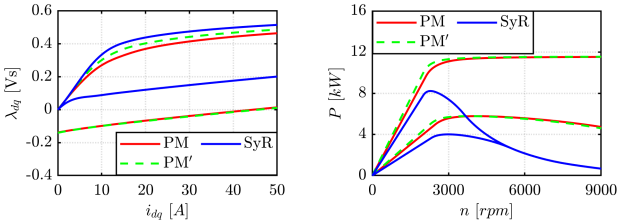

(a) (b)

Fig. 3: Comparison between the final PM-SyR motor with the baseline SyR motor and the PM-SyR motor with virtual PMs: flux linkages (a) and power versus speed at 22 and 44 A (b).

C. Design of the PMs using the Fictituos Remanence B'_r

The PM design is divided in two phases: first, the volume of each flux barrier V'_{PM} is filled with a fictitious magnet of remanence B'_r. The value of B'_r is determined to fulfill the target characteristic current equation (2). Once B'_r is determined, the real PM volume V_{PM} will be calculated, according to the remanence of the real (commercial grade) magnet B_r ($\geq B'_r$), as described in the following.

The value of B'_r determines the PM flux linkage λ_m (see Fig. 2). For the useful B'_r range, the $\lambda_m = \lambda_m(B'_r)$ function can be expressed as:

$$\lambda_m = k_m \cdot B'_r - \lambda_{ribs} \tag{5}$$

Manipulation of (4) and (5) leads to simplify the term λ_{ribs} and to obtain the equation for B'_r:

$$B'_r = \frac{\lambda^{SyR}_{q,i_{ch}}}{k_m} \tag{6}$$

Three FEA simulations are used to solve (6). The first simulation evaluates $\lambda^{SyR}_{q,i_{ch}}$, with the SyR machine supplied at i_{ch} along the q axis. Other two simulations determine the coefficient k_m of the $\lambda_m = \lambda_m(B_r)$ curve, using two different values of B'_r: $B'_{r,A} = 0.3\,T$ and $B'_{r,B} = 0.6\,T$, as depicted in Fig. 2. For the benchmark case, (6) results $B'_r = 0.51\,T$.

D. Final PM Pieces

The dimension of the real PMs is computed using the simple proportional law:

$$V_{PM} = V'_{PM} \cdot \frac{B'_r}{B_r} \tag{7}$$

The equation is applied to each barrier, and the PM volume is adjusted maintaining the PM thickness equal to the barrier thickness for all the barriers. It was shown in [16] that the magnet remanence times volume product determines the open-circuit flux linkage λ_m and therefore the characteristic current of the machine and ultimately all output figures the magnet contributes to.

Now, it is possible to select the PM grade that will be used, in order to compute the PM dimensions (7). A first limit in the PM grade selection comes from B'_r: the remanence of the selected grade should be equal or bigger than B'_r, otherwise the characteristic current will be lower than the target. Another important constraint in the magnet selection is the maximum current before irreversible demagnetization. Usually, two solutions are possible: ferrite PMs or Neodymium PMs. The former presents lower cost, but also a higher risk of demagnetization and lower B_r, that could limit the characteristic current value. Conversely, Neodymium PMs have in general higher remanence and are stronger against demagnetization, but they are more expensive than ferrite PMs and have lower temperature limits. A further comment must be done on centrifugal forces. Ferrite PMs have usually a lower mass density than Neodymium PMs (almost 5 kg/m^3 versus about 7.5 kg/m^3 of Sintered Neodymium PMs). Moreover, the mass of Ferrite PMs required is in general higher than Neodymium PMs because of the remanence difference (around 1.2 T for Neodymium, and about 0.4 T for Ferrite). For this reason, the use of Ferrite magnet in high-speed motors could leads to thicker structural ribs, and so, greater λ_{ribs} and higher PM quantity to saturate them.

E. Regular PM-SyR machine

For the case study, the Ferrite solution is not feasible because of the high B'_r value. The selected PM grade is BMN-38EHS. It is a sintered Neodymium magnet, with a remanence of 1.26 T at 20°C and a maximum operating temperature of 200°C. The cold condition (20°C) is considered for the following analysis to simplify the procedure for the experimental validation. The final geometry of the regular PM-SyR motor is reported in Fig. 5a. Fig. 3 reports the comparison between the final PM-SyR machine (with the real PMs) with the baseline SyR motor and the intermediate PM-SyR design (with barrier completely filled of the virtual PM). The PM insertion slightly lower the λ_d curve (see Fig. 3a) because of the additional saturation in the rotor, caused by the high quantity of magnet needed for i_{ch} target. The additional saturation is more evident for the real PMs because the same flux density is condensed in a smaller region, compared to virtual PMs. The q axis of the PM-SyR machines is perfectly superimposed, validating the procedure. The behaviors of the flux maps are reflected in the power-speed curves (Fig. 3b). The constant power speed range of the SyR machine is strongly improved by the addition of the PMs, as well as maximum power. The two PM-SyR machine have the same characteristics at high speed, while at low speed the higher local saturations effect of the Neodymium PMs are slightly noticeable.

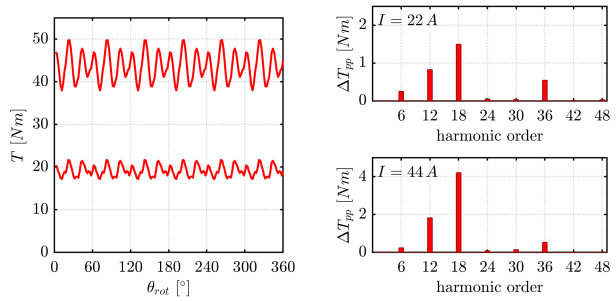

(a) (b)

Fig. 4: Torque of the regular PM-SyR motor: waveform versus rotor position at 22 and 44 A (a) and harmonic components of torque ripple (b) at rated and characteristic current.

III. Torque Ripple Mitigation

Two methods will be considered for torque ripple mitigation: asymmetric rotors and step-skewing. The torque waveform of the regular PM-SyR machine and its harmonic spectrum are reported in Fig. 4 for the two current levels. The specification of Table II are fulfilled: the PM-SyR motor produce $19.16\,Nm$ at $22\,A$ and $43.64\,Nm$ at $44\,A$. As expected, the dominant torque ripple harmonic order equals the number of stator slots per pole pair 18. It follows that the target torque ripple harmonic, objective of the torque ripple minimization, will be $h = n_s = 18$.

A. Flux Barrier Shift

Several methods to reduce torque ripple using asymmetric rotors are available in literature [7] - [10]. The FBS method adopted in the following was successfully applied to SyR machine in the recent past [12]. This technique acts on each pair of poles of the rotor (see Fig. 5) by shifting the d axis half way of the two poles by the angle θ_{FBS}. The rotor barriers ends of the two half poles before and after the said d axis do shift of the same quantity, whereas the barriers ends of the remaining half poles (extreme left and right) do not move. The result is that one pole (left in the figure) is wider and the other one is narrower than the average pole pitch. Since the asymmetry refers to the electrical period, the rotor is still mechanically symmetric and unbalanced magnetic pull is minimal. Furthermore, the angular span between the q positive and negative axes is still 180 electrical degree, while this is not true for the d axis. Also the PM pieces of the two asymmetric poles are equal. Besides the modified lamination geometry, the manufacturing process has no extra complication respect to the case of the regular rotor.

The shift angle can be analytically computed as [12]:

$$\theta_{FBS} = \frac{360}{2 \cdot p \cdot h} \tag{8}$$

Where h is the target torque harmonic that should be reduced. For the considered machine, $h = n_s = 18$ and so $\theta_{FBS} = 5°$.

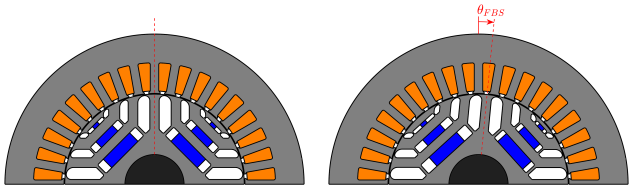

(a) (b)

Fig. 5: Geometry of the final PM-SyR machines: regular version (a) and asymmetric version, with $\theta_{FBS} = 5.5°$ (b).

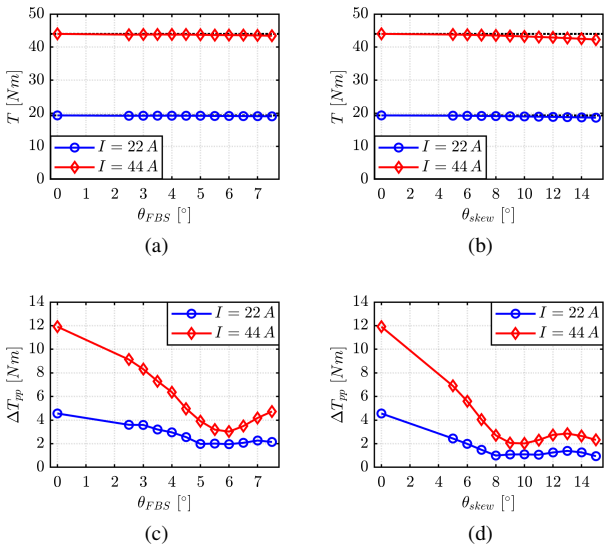

(a) (b) (c) (d)

Fig. 6: Torque ripple reduction optimization at $I = 22\,A$ (blue curves) and $I = 44\,A$ (red curves). Torque versus θ_{FBS} (a) and versus θ_{skew} (b); and torque ripple versus θ_{FBS} (c) and versus θ_{skew} (d).

B. Step-skewing

The most common method to reduce torque ripple is step-skewing. With this method, the rotor is divided into a finite number of axial slices. They are regularly shifted in order to have an angular span between the first and the last slice equal to the skew angle θ_{skew}. This angle can be computed as:

$$\theta_{skew} = \frac{360}{p \cdot h} \tag{9}$$

With $h = n_s = 18$, the skew angle is equal to $\theta_{skew} = 10°$. Skewing drastically reduce torque ripple, but involves complication of the manufacturing process.

C. Optimization of skew and FBS angles

Considering that torque ripple has more than one harmonic order (see Fig. 4), the shift and skew angles can be further optimized. To find the best angles for the two methods, average torque and torque ripple are computed for several values of θ_{FBS} and θ_{skew}, for two current levels: $22\,A$ (thermal rated current) and $44\,A$ (characteristic current). The results of the sensitivity analysis are reported in Fig. 6 with the blue curves representing the rated current and the red curves the

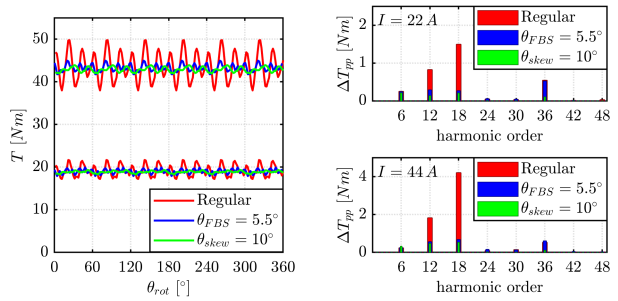

Fig. 7: Comparison of the regular PM-SyR motor (red) with the FBS motor (blue) and the skewed one (green): torque waveforms (a) and torque ripple harmonics (b) at 22 A and 44 A.

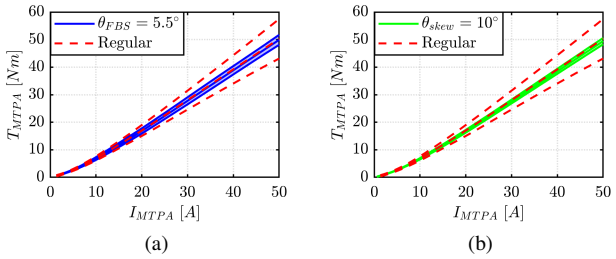

Fig. 8: Comparison of the MTPA torque: Flux Barrier Shift (a) versus Step-Skewing (b). The regular machine is superimposed with black dashed lines.

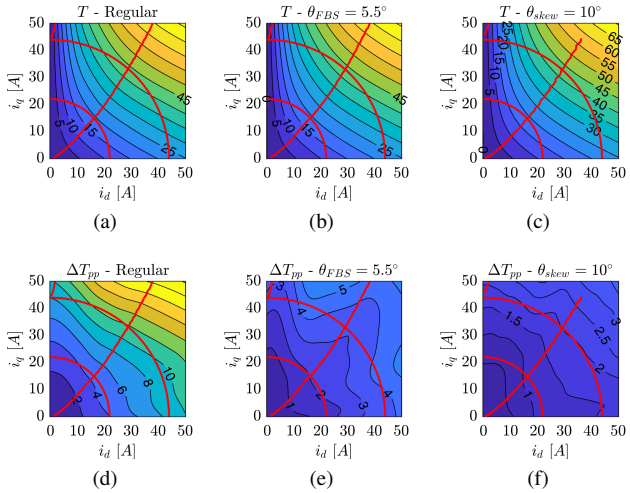

Fig. 9: Maps on the i_d, i_q plane: torque of regular (a), FBS (b) and skewed (c) machine and peak-to-peak torque ripple of regular (d), FBS (e) and skewed (f) machine. Red curves shows MTPA, MTPV, rated and characteristic current

characteristic current conditions. The analysis highlights that the nominal values $\theta_{FBS} = 5°$, $\theta_{skew} = 10°$ are very close to the minimum torque ripple ones. In general skewing is slightly more effective than FBS in torque ripple reduction (see Fig. 6c-d), but has lesser impact on average torque (see Fig. 6a-b).

Upon sensitivity analysis, the optimal angles, selected for further investigations are $\theta_{FBS} = 5.5°$ and $\theta_{skew} = 10°$.

IV. FEA Comparison between FBS and Skewing

The pros and cons of FBS and skewing are investigated, using the regular PM-SyR motor performance as a term of comparison. The first figure under comparison is obviously the output torque, whose waveform is represented in Fig. 4 along with the torque ripple spectrum. Average torque and peak to peak ripple versus current amplitude under Maximum Torque per Ampere (MTPA) conditions are also compared for the two machines, and finally the same figures are compared across the entire i_d, i_q plane. Finally, the significant figures of demagnetization current limit and efficiency maps are also analyzed and compared.

A. Torque Waveforms

Torque waveforms at rated and characteristic current are computed for the two machines. Fig. 7a shows the torque wave at the two current levels and Fig. 7b report the torque ripple spectrum. The improvements from the regular PM-SyR motor are evident. Torque ripple is reduced at about $1/3$ from FBS and about $1/4$ from skewing. The target torque harmonic $h = 18$ presents the highest reduction, with a residual component less than $1/6$ than the regular rotor one. Regarding average torque, skewing reduce torque of about 2% for both current conditions, while FBS maintain the same output torque of the regular machine.

B. Torque versus Current at MTPA conditions

The previous analysis is extended to the whole MTPA locus. Fig. 8 shows the torque versus current along the MTPA for the asymmetric (Fig. 8a) and skewed (Fig. 8b) motor. Torque ripple band is included on the plot, as well as the regular motor curve (dashed red lines). The properties highlighted from the previous analysis are confirmed on the whole current range. Torque ripple is drastically reduced from both methods, with a slightly advantage of skewing. Average torque is unchanged from FBS (blue line of Fig. 8a copy the red dashed line), while skewing reduces average torque, with a more evident effect at high current levels.

C. Torque Maps in the i_d, i_q Domain

The analysis domain is further extended to the entire i_d, i_q plane. Fig. 9 shows the torque and torque ripple maps for the three machines. MTPA trajectories are reported in red, as well as the two current levels. As for the previous analysis, torque differences are limited, with a slightly penalization for skewing. Conversely, torque ripple is strongly reduced over the entire dq plane. In addition, the FBS motor map presents a peculiar feature: torque ripple surface has a sort of valley around the MPTA, index of an optimal torque ripple reduction in the working conditions at low speed.

D. Demagnetization Current Versus PM Temperature

Demagnetization current is one of the limits to be considered for all PM Synchronous Machines. The maximum allowed current is affected by the PM temperature, as the

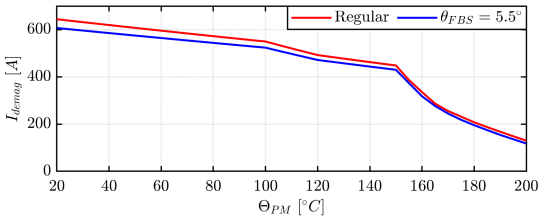

Fig. 10: Demagnetization current versus magnet temperature for regular (red) and FBS (blue) rotor.

coercivity of NdFeB magnets decreases with temperature increase. Skewing does not reduce the demagnetization current respect to the regular machine case, because each slice is equal to the regular machine. Conversely, the FBS changes the laminations geometry, with a possible augmented risk of demagnetization. Fig. 10 reports the demagnetization curve for the regular and shifted rotor. The PMs temperature is reported on the x-axis, while the maximum admissible current (in steady-state) is reported on the y-axis. The demagnetization limit of the asymmetric poles machine is slightly lower than the one of the skewed machine, equal to the one of the regular machine. However, for both machines the demagnetization current at $200°C$ is circa three-times the characteristic current, and at $\Theta_{PM} = 150°C$, the demagnetization limit is 10 times the characteristic current. It follows that all the possible working conditions, for all the considered rotor are safe against demagnetization.

E. Efficiency Maps

The last comparison between the three machines regards the efficiency map in the torque-speed plane. Fig. 11 shows the efficiency maps computed for the three PM-SyR motors with the voltage and current limits reported in Table II. The control strategy adopted is the maximum efficiency locus. It means that the control algorithm, for each torque and speed, compute the loss map in the dq plane and select the best working point in terms of efficiency, that fulfill the current and voltage limits. Regular and FBS motor presents almost the same characteristic, while the skewed machine has a lower efficiency. This analysis confirms the negligible effect of FBS on the machine model: only torque ripple is reduced, while torque, flux linkage and loss are maintained. Conversely, skewing increase copper loss, because of the higher current needed to reach the same torque, and iron loss because of the different working point among the axial slices.

V. Experimental Validation of FBS

To further validate the procedure, two prototypes are built and tested. They are the regular PM-SyR motor and the FBS motor, with $\theta_{FBS} = 5.5°$ (see Fig. 5). The experiments have two objectives. The first is to demonstrate that the FBS procedure is effectively able to reduce torque ripple without changing the average output torque. The second aim is to investigate the precision of the design tools. This second aspect is more critical because involves all the problems that could

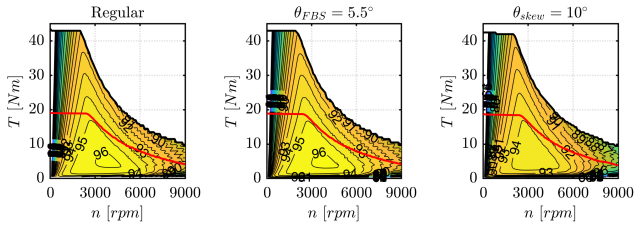

Fig. 11: Efficiency maps of regular (a), FBS (b) and skewed (c) motor. Red curve highlight the torque envelop for rated current.

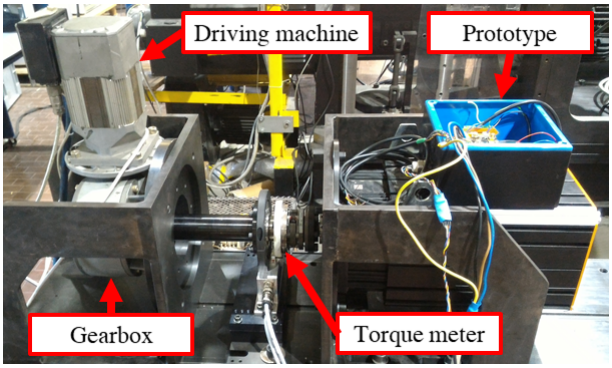

Fig. 12: Picture of the test rig for torque ripple measurement.

arise from the manufacturing process and will be useful in the future applications of the method.

Two identifications are preformed on the two prototypes: magnetic model identification and torque ripple map. Fig. 12 shows a picture of the FBS prototype on torque ripple test rig. The prototype is current controlled using a custom inverter, while the speed is imposed by a driving machine. An HBM Gen7t-a data acquisition system collects all the electrical and mechanical quantities. For the torque ripple measurement, a worm screw reducer is placed between the driving machine and the torque meter. This addition is done because, during the torque ripple measurement, speed must be kept constant at very low values (10 rpm). The gearbox helps to satisfy this requirement by enabling the driving machine to work at the rated speed, where the speed loop works better. Plus, all the speed oscillations from the driving machine are filtered with the reduction ratio, making the prototype speed constant and rejecting torque ripple from the driving machine.

A. Torque Waveforms

The first experimental validation deals with torque waveforms. Fig. 13a shows the torque waveforms of the two prototypes measured on torque ripple test rig. The torque ripple reduction from the regular prototype (red curves) to the FBS prototype (blue curves) is evident. Fig. 13b reports the FEA results of the measured working points. The main difference is a general overestimation of torque for both motors of about 10%. To investigate this discrepancy, further tests must be done.

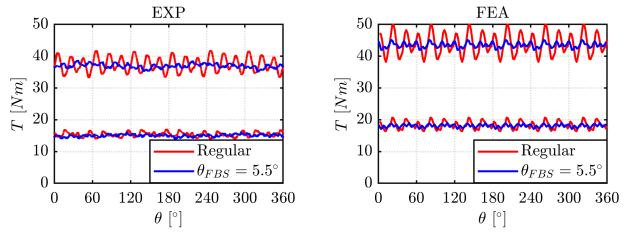

Fig. 13: Torque waveforms measured from the two prototypes (a) and simulated with FEA (b) at 22A and 44A.

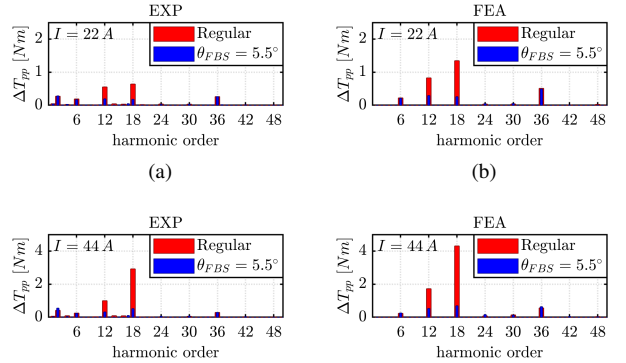

Fig. 14: Torque ripple harmonics from experimental measurements at 22A (a) and 44A (c) and from FEA simulations at 22A (b) and 44A (d).

Considering the torque ripple harmonics, the trends resulting from the simulations are almost confirmed. Fig. 14 shows the torque ripple harmonics for the two prototypes at the two considered current levels. The FEA results are reported in subfigure (b) and (d) for a sake of comparison. FEA tends to overestimate torque ripple, too. Moreover, the capability of FBS to reduce the higher torque ripple harmonics is confirmed from the experimental results. The experiments highlight also a second order harmonic on torque for both prototypes, that is caused by some problems in the manufacturing process of the two machines.

B. Magnetic Model

To investigate the discrepancy between FEA and experiments, the first check is on the magnetic model. The identification is performed following the procedure described in [17]. The driving machine keep the speed constant at 500 rpm, while the prototype explores a regular grid in the i_d, i_q plane. The results of this test are the flux linkages maps, function of the dq currents. Fig. 15 shows the flux curves measured from the two machines (solid lines) compared with the FEA results (dashed lines). To simplify the plot, only the extreme curves are plot, and so $\lambda_d(i_d, 0)$ and $\lambda_q(0, i_q)$. From the analysis results that FEA always overestimate λ_d and underestimate λ_q. Mechanical tolerances during the manufacturing process can partially justify the discrepancy. Furthermore, laser cut damage the lamination, worsening the magnetic characteristic [18].

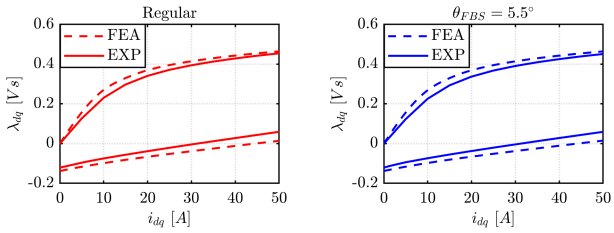

Fig. 15: Comparison between the FEA-evaluated (dashed lines) and the experimental measured (solid lines) flux curves for regular (a) and asymmetric (b) motor.

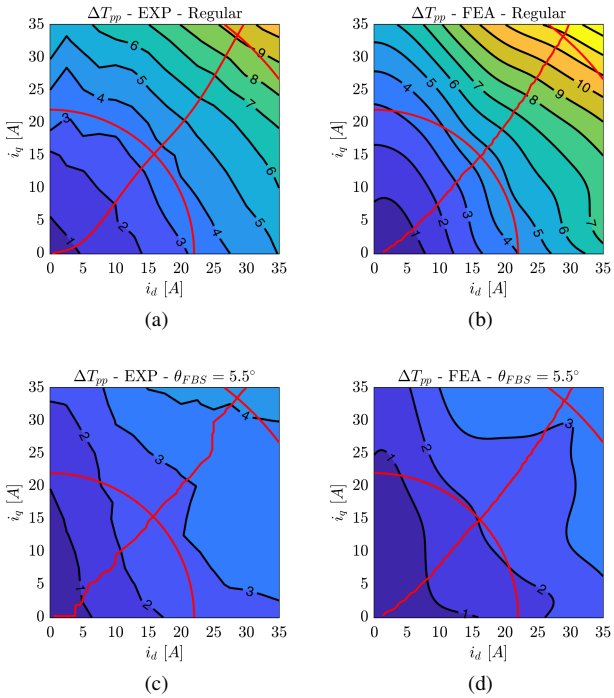

Fig. 16: Torque ripple maps measured on the regular (a) and asymmetric (c) prototype, compared with the FEA-evaluated torque ripple maps.

Besides the manufacturing problems, no noticeable differences are visible between the experimental flux maps of the two prototypes, confirming the insensitivity of the magnetic model to FBS procedure.

C. Torque Ripple Maps

The next step in the validation regards torque ripple maps. Fig. 16 reports the results of the torque ripple map on regular and asymmetric machine (subfigure a and c respectively), compared with the FEA simulations (subfigures b and d). Toque ripple is effectively reduced over the entire dq plane, as expected. Regarding FEA precision, torque ripple is better estimated than torque. A further comment must be done on the FBS prototype measures: for this motor, torque ripple is close to the instrument precision and so a worst match with FEA is partially acceptable.

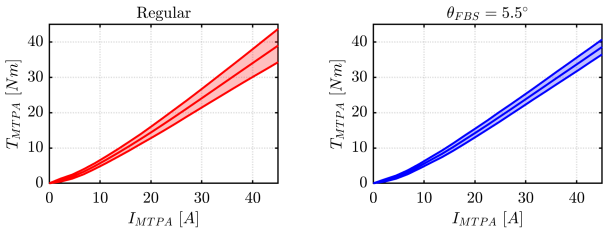

(a) (b)

Fig. 17: Measured torque versus current along the MTPA for regular (a) and shifted (b) prototype with torque ripple band.

D. Torque Capability along the MTPA

To summarize the benefits of FBS procedure and better visualize the differences between the two prototypes, the MTPA curves are compared. Fig. 17 reports the measured torque capability of the two prototypes, with torque ripple band superimposed. The FBS properties are clearly visible in the pictures: torque is unchanged from FBS, while torque ripple band is narrowed over the entire current range. The FBS behaviors are experimentally confirmed.

VI. Conclusions

A fast design procedure to design low-torque-ripple PM-SyR machine is presented. The design flowchart is divided into three steps: first the baseline SyR machine, with the overall machine dimensions is designed. The PMs are designed according to the characteristic current and last torque ripple is minimized.

About torque ripple reduction, two techniques are compared: FBS and skewing. Both shift and skew angle are optimized and the best machines are compared with the regular motor. Asymmetric rotor results slightly less effective than skewing in torque ripple reduction, but ensure the preservation of the other performance figures as output torque and efficiency and the easiness of the manufacturing process.

To further validate the FBS design, two prototypes was built and tested. The regular rotor is experimentally compared to the asymmetric rotor and the measurements confirms the FBS behaviors: torque ripple is minimized without additional drawbacks.

References

[1] F. Momen, K. Rahman, and Y. Son, "Electrical propulsion system design of Chevrolet Bolt battery electric vehicle," *IEEE Transactions on Industry Applications*, vol. 55, no. 1, pp. 376–384, Jan 2019.

[2] G. Y. Sizov, D. M. Ionel, and N. A. O. Demerdash, "Modeling and design optimization of PM AC machines using computationally efficient - finite element analysis," in *2010 IEEE Energy Conversion Congress and Exposition*, Sep. 2010, pp. 578–585.

[3] K. Yamazaki and Y. Togashi, "Shape optimization procedure of interior permanent magnet motors considering carrier harmonic losses caused by inverters," *IEEE Transactions on Magnetics*, vol. 54, no. 3, pp. 1–4, March 2018.

[4] E. C. Lovelace, T. M. Jahns, and J. H. Lang, "A saturating lumped-parameter model for an interior PM synchronous machine," *IEEE Transactions on Industry Applications*, vol. 38, no. 3, pp. 645–650, May 2002.

[5] W. L. Soong and T. J. E. Miller, "Field-weakening performance of brushless synchronous AC motor drives," *IEE Proceedings - Electric Power Applications*, vol. 141, no. 6, pp. 331–340, Nov 1994.

[6] A. Vagati, G. Franceschini, I. Marongiu, and G. P. Troglia, "Design criteria of high performance synchronous reluctance motors," in *Conference Record of the 1992 IEEE Industry Applications Society Annual Meeting*, Oct 1992, pp. 66–73 vol.1.

[7] E. Howard, M. J. Kamper, and S. Gerber, "Asymmetric flux barrier and skew design optimization of reluctance synchronous machines," *IEEE Transactions on Industry Applications*, vol. 51, no. 5, pp. 3751–3760, Sep. 2015.

[8] T. Lange, B. Kerdsup, C. Weiss, and R. W. De Doncker, "Torque ripple reduction in reluctance synchronous machines using an asymmetric rotor structure," in *7th IET International Conference on Power Electronics, Machines and Drives (PEMD 2014)*, April 2014, pp. 1–5.

[9] N. Bianchi, S. Bolognani, D. Bon, and M. Dai Pre, "Rotor flux-barrier design for torque ripple reduction in synchronous reluctance and PM-assisted synchronous reluctance motors," *IEEE Transactions on Industry Applications*, vol. 45, no. 3, pp. 921–928, May 2009.

[10] M. Sanada, K. Hiramoto, S. Morimoto, and Y. Takeda, "Torque ripple improvement for synchronous reluctance motor using an asymmetric flux barrier arrangement," *IEEE Transactions on Industry Applications*, vol. 40, no. 4, pp. 1076–1082, July 2004.

[11] M. Davoli, C. Bianchini, A. Torreggiani, and F. Immovilli, "A design method to reduce pulsating torque in PM assisted synchronous reluctance machines with asymmetry of rotor barriers," in *IECON 2016 - 42nd Annual Conference of the IEEE Industrial Electronics Society*, Oct 2016, pp. 1566–1571.

[12] S. Ferrari, G. Pellegrino, M. Davoli, and C. Bianchini, "Reduction of torque ripple in synchronous reluctance machines through flux barrier shift," in *2018 XIII International Conference on Electrical Machines (ICEM)*, Sep. 2018, pp. 2290–2296.

[13] F. Cupertino, G. Pellegrino, and et al., "SyR-e: Synchronous Reluctance (machines) - evolution," accessed 24-January-2019. [Online]. Available: https://sourceforge.net/projects/syr-e/

[14] S. Ferrari and G. Pellegrino, "FEA-augmented design equations for synchronous reluctance machines," in *2018 IEEE Energy Conversion Congress and Exposition (ECCE)*, Sep. 2018, pp. 5395–5402.

[15] R. Leuzzi, P. Cagnetta, S. Ferrari, P. Pescetto, G. Pellegrino, and F. Cupertino, "Transient overload characteristics of PM-assisted synchronous reluctance machines, including sensorless control feasibility," *IEEE Transactions on Industry Applications*, vol. 55, no. 3, pp. 2637–2648, May 2019.

[16] B. Boazzo, A. Vagati, G. Pellegrino, E. Armando, and P. Guglielmi, "Multipolar ferrite-assisted synchronous reluctance machines: A general design approach," *IEEE Transactions on Industrial Electronics*, vol. 62, no. 2, pp. 832–845, Feb 2015.

[17] E. Armando, R. I. Bojoi, P. Guglielmi, G. Pellegrino, and M. Pastorelli, "Experimental identification of the magnetic model of synchronous machines," *IEEE Transactions on Industry Applications*, vol. 49, no. 5, pp. 2116–2125, Sep. 2013.

[18] P. Lazari, K. Atallah, and J. Wang, "Effect of laser cut on the performance of permanent magnet assisted synchronous reluctance machines," *IEEE Transactions on Magnetics*, vol. 51, no. 11, pp. 1–4, Nov 2015.